A sustainable strategy to prepare porous carbons with tailored pores from shrimp shell for use as supercapacitor electrode materials

GAO Feng[1], XIE Ya-qiao[2], ZANG Yun-hao[1], ZHOU Gang[1], QU Jiang-ying[1,*], WU Ming-bo[3,*]

（1. *School of Environment and Civil Engineering*, *Dongguan University of Technology*, *Dongguan* 523808, *China*;
2. *College of Chemistry and Chemical Engineering*, *Liaoning Normal University*, *Dalian* 116029, *China*;
3. *Institute of New Energy*, *State Key Laboratory of Heavy Oil*, *China University of Petroleum (East China)*, *Qingdao* 266580, *China*）

Abstract: The highly efficient synthesis of nitrogen-doped carbons with different pore structures is reported using shrimp shell as the carbon and nitrogen source, and its $CaCO_3$ component as the hard template and activator. The $CaCO_3$ content of shrimp shells can be easily changed by changing the leaching time to remove it. $CaCO_3$ acts as the activator and template to tailor the pore sizes of the carbons. CO_2 from the decomposition of $CaCO_3$ also plays an activating role. Their specific surface areas, pore volumes, ratios of micropore volume to total pore volume can be adjusted in the ranges 117.6-1 137 $m^2\ g^{-1}$, 0.14-0.64 $cm^3\ g^{-1}$, and 0-73.4%, respectively. When used as the electrodes of a supercapacitor, the porous carbon obtained with a leaching time of 92 min has a high capacitance of 328 F g^{-1} at 0.05 A g^{-1} in a 6 mol L^{-1} KOH electrolyte and 619.2 F g^{-1} at 0.05 A g^{-1} in a 1 mol L^{-1} H_2SO_4 electrolyte. Its corresponding energy density at a power density of 1 470.9 W kg^{-1} is 26.0 Wh kg^{-1}. This study provides a low cost method for fabricating porous carbons from biomass with a high added value.

Key words: Strategy of functional assembly; Self-activation; Pore structures tailoring; Porous carbon; Supercapacitor

1 Introduction

The environment-friendly energy storage devices have attracted much attention because of the increasing global warming and depletion of oil reserves[1, 2]. Supercapacitors are considered to be potential energy storage devices with short charging time, long cycle life and high power density[3–5], which include the electrostatic double layer capacitors (EDLCs) and the pseudo-capacitors. Porous carbons with the advantages of the high specific surface area and the moderate cost are currently a good choice for supercapacitor electrodes[6–9]. The researchers have demonstrated that the capacitance of the carbon electrodes depends on their porous structures and surface properties[9–12]. Although the developments of carbon-based supercapacitors are encouraging, constructing different scaled pores of carbons with the sustainable synthetic strategies need to be studied in detail.

To date, well-defined porous carbons are accessible by activation methods and/or template methods with the different precursors. The most commonly used method for the synthesis of porous carbons is the activation method, which combines with the high temperature calcination of the mixtures of the carbon precursor and the activator such as KOH, $ZnCl_2$, H_3PO_4[13, 14]. For example, Zhu et al.[15] prepared a microporous carbon with a specific surface area of up to 1 776.9 $m^2\ g^{-1}$ by KOH activation using a micro-structured skunk as the carbon source, which showed a high specific capacitance of 213.4 F g^{-1} in 1 mol L^{-1} H_2SO_4 even at a current density of 20 A g^{-1}. Generally, the acid/base activation technique suffers from the disadvantage such as the environmental pollution and the apparatus corrosion. The template method provides another way for the fabrication of tunable porous carbons with the nanostructured zeolite, ZnO, Al_2O_3, $Mg(OH)_2$ or mesoporous SiO_2 as the hard templates impregnated with the appropriate carbon precursors[16–19], which often involves dipping, curing, calcining and template removal processes. As a result, the porous carbon can be obtained with well-defined topologies and pore dimensions that depend on the kind and morphology of hard templates. The disadvantages of such synthesis include the fussy and time-con-

Received date: 2020-09-22; **Revised date:** 2020-11-28

Corresponding author: QU Jiang-ying, Professor. E-mail: qujianggaofeng@163.com;
WU Ming-bo, Professor. E-mail: wumb@upc.edu.cn

Author introduction: GAO Feng, Associate professor. E-mail: fenggao2003@163.com

suming procedure, the massive used hazardous substances, and the tedious removal of the hard templates.

Alternatively, a sustainable and scalable strategy for the preparation of porous carbon has been proposed. For example, Yang et al.[20] reported NaCl-template synthesis of carbon with rich mesopores and macropores, where NaCl as the soluble salt is less expensive than common templates used, and it is easy to remove by water washing because of its high solubility. But the resultant carbon exhibited a low specific surface area and its porous structure was difficult to precisely regulate. Guo et al.[21] reported carbon spheres synthesized by $CaCO_3$ template-induced activation of dopamine, which exhibited a large specific surface area of up to 1 984 $m^2\ g^{-1}$ and 7.57% nitrogen doping level. Instead of commercial templates, White et al.[22] pioneered to synthesize mesoporous carbons with the surface area of 177-328 $m^2\ g^{-1}$ using the intrinsic $CaCO_3$ in the prawn shell as the self-template. Inspired by his work, our group has well developed above method to synthesize adjustable porous carbons using shrimp shell as the precursor. For instance, the self-template method combined with H_3PO_4 activation of shrimp shell produced a N, P, O doped porous carbon with a surface area of 774 $m^2\ g^{-1}$[23], while KOH activation resulted in a surface area of 2 032 $m^2\ g^{-1}$[24]. Above two kinds of samples showed the good performances as the electrode materials for the supercapacitors, the specific capacitance of which reached 206 and 328 F g^{-1} in 6 mol L^{-1} KOH electrolyte at 0.1 A g^{-1}, respectively. Such a self-template combined with activation approach for the synthesis of micro/mesoporous carbons also involved the additional activation agents. Therefore, it also raised the cost of production, and caused the corrosion of equipment and serious environmental pollution. Furthermore, the reported work only focused on natural $CaCO_3$ as the template for the synthesis of porous carbon. However, $CaCO_3$ can be calcined at high temperature to produce CaO, the role of which in regulating porous structure of carbon need to be investigated in detail. Recently, we reported the synthesis of porous carbon directly using oyster shells with a $CaCO_3$ content of 96.1% as both activation agent and the template, and a soft pitch as the carbon precursor[10]. It was found that CaO produced by the thermal decomposition of $CaCO_3$ could be used as the self-activation agent, which helped to produce a series of porous carbons with the surface area of 612-1 258 $m^2\ g^{-1}$ by tailoring the ratio of oyster shells and soft pitch. When used as the electrode of a lithium ion battery, a typical porous carbon exhibited a reversible capacity of 1 251 mAh g^{-1}. Such work provided an environment friendly method for the synthesis of porous carbon for the energy storage to fulfill the high-value added use of oyster shell. Because of the high content of $CaCO_3$ in the oyster shells, additional carbon source was necessary to produce porous carbons. Based on the reported work, the synthesis of porous carbons with tailored pore sizes using one typical biomass as the trinity of carbon source, hard template and activator remains a challenge.

Herein, we select the waste shrimp shells as the only source to synthesize porous carbons with the tailored pore sizes. The effect of the pore structures on the performance of supercapacitors is also investigated. It is known that shrimp shell contains about 40% nitrogen polysaccharide chitin and protein, and about 60% inorganic $CaCO_3$. The former can be used as the nitrogen/carbon source for the synthesis of nitrogen-doped carbons, which will contribute to pseudocapacitance for the use as the supercapacitor electrode. The latter can be used as both the template and the activator for in-situ tailoring the pore sizes of the carbons for the EDLCs. The major challenge in this case is how to fabricate a porous carbon with tailored pore size by a sustainable route without the assistance of additional activator.

2 Experimental

2.1 Synthesis of shrimp shell derived N-doped porous carbons

Bohai shrimp shell was used as the source. The N-doped porous carbons were synthesized by selective demineralization, followed by self-activation at high temperature. Firstly, 7.08 g dried shell was dispersed in 50 mL of a 20% acetic acid (HAc) solution

for different times to selective removal of its intrinsic $CaCO_3$. The samples were afterwards washed with deionized H_2O until neutral pH and dried at 80 °C. Secondly, the dried samples were calcinated at 900 °C for 3 h with a heating rate of 5 °C min^{-1} under nitrogen flow. Finally, the obtained samples were adequately dissolved in a 20% HAc at room temperature until CaO residue derived from $CaCO_3$ was completely removed. Then samples were completely reclaimed by filtration and rinsed with deionized water until the solution became neutral and dried overnight at 80 °C. A series of samples were obtained and designated as C-X $CaCO_3$ (X is the percentage of remaining $CaCO_3$ in the samples). For comparison, C-100% $CaCO_3$ was synthesized by a similar procedure without the demineralization step.

2.2 Characterization

The morphologies and microstructures of the as-acquired products were inspected using field emission scanning electron microscopy (SEM, Hitachi Ltd SU8010), X-ray photoelectron spectroscopy (XPS, Thermo VG Scientific Sigma Probe Spectrometer) and thermogravimetric analysis (TG). The Brunauer-Emmett-Teller (BET) surface area of the carbon samples was determined by physisorption of N_2 at 77 K using a Micromeritics ASAP 2020 analyzer.

2.3 Electrochemical measurements

The supercapacitors were assembled according to the literatures[25, 26]. The electrochemical properties of the samples were estimated by a CHI660C electrochemical work station in a three-electrode cell. Hg/HgO and Hg/Hg_2SO_4 electrodes were used as the reference electrodes in 6 mol L^{-1} KOH and 1 mol L^{-1} H_2SO_4 aqueous electrolytes, respectively. In both case, platinum foil was employed as the counter. The mass ratio of the active materials, carbon black, and polytetrafluoroethylene (PTFE) in the working electrode was 75∶20∶5. The active mass was averagely 1.5 mg per electrode. Before testing, the prepared electrodes were soaked overnight in the electrolyte. The CV measurements were performed in a potential window between −0.1 and −0.9 V in 6 mol L^{-1} KOH and −0.7-0.3 V in 1 mol L^{-1} H_2SO_4. The electrochemical impedance spectroscopy (EIS) measurements were recorded on a CHI 660C electrochemical work station in a frequency range from 100 kHz to 0.01 Hz. The long-term cycling performance of the C-25% $CaCO_3$ electrode was measured by the consecutive galvanostatic charge-discharge in 6 mol L^{-1} KOH and 1 mol L^{-1} H_2SO_4 solution at current density of 1 A g^{-1} on a Land CT2001A cycler at room temperature. The assembly of the supercapacitor with two symmetrical work electrodes was tested at different cell voltages. The electrolyte was 6 mol L^{-1} KOH with nickel foam as a current collector and 1 mol L^{-1} H_2SO_4 solution with titanium mesh as a current collector.

The specific capacitances were calculated as the following equations:

$$C_S = \frac{I \times \Delta t}{\Delta V \times m} \tag{1}$$

where C_s is the specific capacitance (F g^{-1}), I is the galvanostatic discharge current (A), Δt is the discharging time (s), ΔV is the potential window during discharge, and m is the mass of the active materials in the working electrode (g).

$$E = \frac{C_S \times \Delta V^2}{7.2} \tag{2}$$

$$P = \frac{3600 \times E}{\Delta t} \tag{3}$$

where E and P are the energy density (Wh kg^{-1}) and power density (W kg^{-1}), respectively. C_s is the specific capacitance (F g^{-1}) of the two electrodes and ΔV is the working voltage for devices (V).

3 Results and discussion

Fig. 1 shows the whole green strategy of self-activation of shrimp shell for N-doped porous carbons with tailored pores for the supercapacitors. Herein, the intrinsic $CaCO_3$ can act as the mesoporous template, and the CaO activator derived from the pyrolysis of $CaCO_3$ can tailor micropores of the obtained carbons. The content of $CaCO_3$ in shrimp shell plays an important role, which can be regulated to be 0, 25% and 50% after 150, 92 and 30 min by leaching with 20% HAC, respectively. For comparison, pristine shrimp shell without any HAC treatment was used. All shrimp shell samples with different $CaCO_3$ contents were car-

bonized at 900 °C in N_2 atmosphere followed by the removal of CaO using a HAC solution. $Ca(AC)_2$ as the by-product could be used as the calcium supplement. The resultant carbon samples with tailored pores were used as supercapacitor electrodes. Different from other strategies including soft/hard-template and activation methods for the synthesis of N-doped porous carbons[16, 17], the feature of this work is that shrimp shell are the only source for the synthesis of porous carbons without any additional activator, template and carbon source involved.

Fig. 2 shows temperature-dependent decomposition of shrimp shell in air by TGA and the demineralization process of shrimp shell with 20% HAC for different times. The mass change of shrimp shell from 10 to 900 °C was tested at a heating rate of 10 °C min^{-1}, as shown in Fig. 2a. The loss of water below 300 °C is approximately 5.7%. The significant mass loss occurred in the range of 300-430 °C is attributed to the decomposition of organic compounds. The loss occurred in the range of 430-600 °C is believed to be the further decomposition of organic compounds, the carbon combustion and the decomposition of $CaCO_3$ to form CaO[27, 28]. The weight remains stable until 800 °C, indicating the complete decomposition of $CaCO_3$ and the formation of CaO with a content of 34.5%. It can be calculated that the $CaCO_3$ content in the shell is about 61.6%. The shrimp shell with different contents of $CaCO_3$ in the range of 0, 25%, 50%, 100% can be tailored by different leaching times using 20% HAC (Fig. 2b), which can be used as the template and activator for the synthesis of porous carbons.

Fig. 3 shows the SEM images of raw shrimp shell, shrimp shell after complete removal of $CaCO_3$

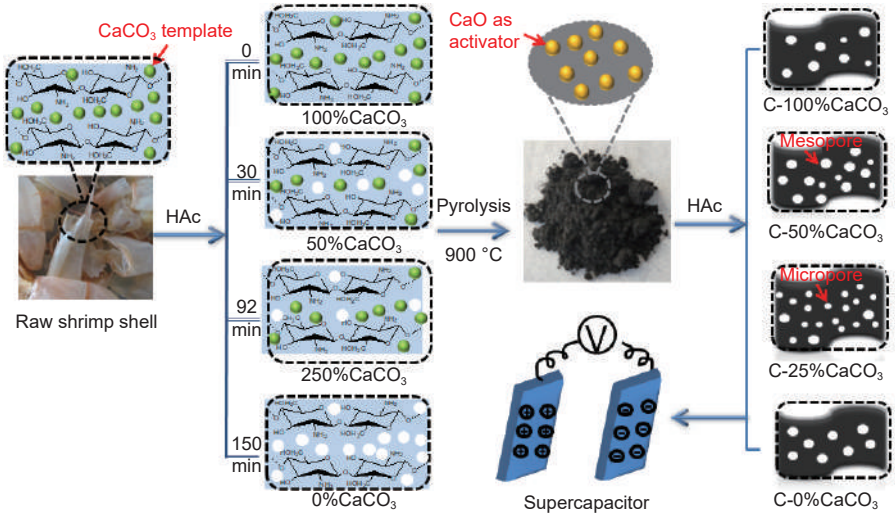

Fig. 1　Schematic of N-doped carbon synthesis with tailored pore sizes from shrimp shell for supercapacitors.

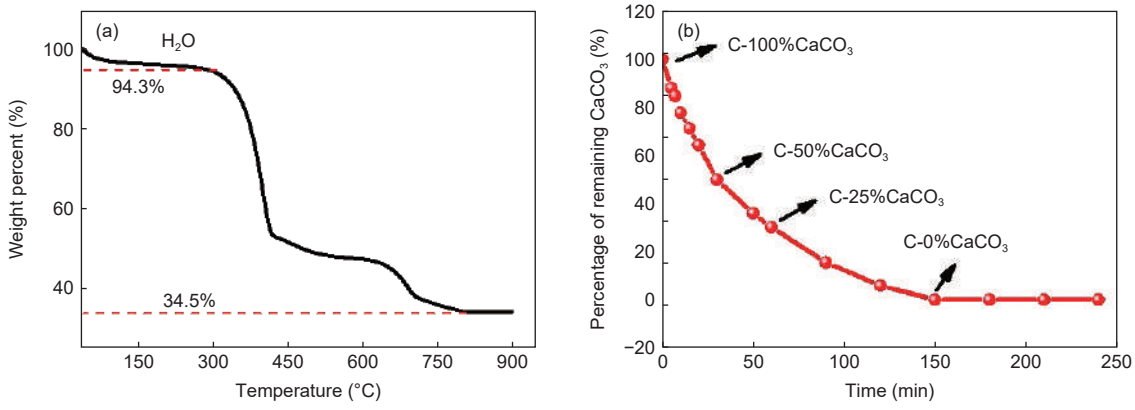

Fig. 2　(a) TGA curve of the shrimp shell in air and (b) the percentage of remaining $CaCO_3$ of the shrimp shell with the variation times after leaching with 20% HAC.

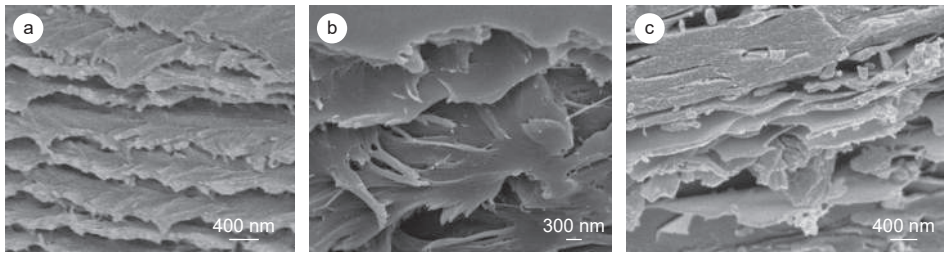

Fig. 3 SEM images of (a) raw shrimp shell, (b) shrimp shell after the complete removal of $CaCO_3$ and (c) C-25% $CaCO_3$ sample.

and C-25% $CaCO_3$ samples. The raw shrimp shell exhibits a stacked layer morphology as shown in Fig. 3a. Fig. 3b demonstrates that the product also remains the layered structure even after the complete removal of $CaCO_3$, indicating that organic skeleton has been strongly built in the sheet structure. As expected, layered sheets of C-25% $CaCO_3$ sample are preserved after high-temperature calcination for the removal of most oxygen and nitrogen of the precursor as shown in Fig. 3c. Such structure is beneficial to ion transport and capacitance increase of the samples. During the transition of shrimp shell into porous carbons, CaO derived from $CaCO_3$ always exits in the carbon skeleton to produce the porous structure, which will be discussed by N_2 adsorption-desorption isotherms.

The N_2 adsorption-desorption isotherms and corresponding pore size distributions are further used to investigate the porosity of the obtained samples, as shown in Fig. 4. The detailed porous properties of the carbons derived from shrimp shell are also listed in Table 1. It is found that the content of $CaCO_3$ in the precursor plays an important role on the porous structures of the resultant samples. When $CaCO_3$ in shrimp shell is completely removed by HAC, the obtained carbon named as C-0% $CaCO_3$ exhibits characteristics of a type IV isotherm, indicating C-0% $CaCO_3$ possesses a mesoporous structure with a specific surface area (S_{BET}) of 117.6 $m^2\ g^{-1}$. The mesopores are derived from the piled pores of the carbon particles and the residual pores after the removal of $CaCO_3$. When the content of $CaCO_3$ is retained to 25% in shrimp shell, the obtained C-25% $CaCO_3$ displays a type I adsorption isotherm with a high S_{BET} of 1 371 $m^2\ g^{-1}$, where microporous and mesoporous specific surface areas (S_{Mic}) and (S_{Mec}) are 1 114 and 257.8 $m^2\ g^{-1}$, respectively. It should be noted that S_{Mic} is about 12 times higher than that of C-0% $CaCO_3$. Such an obvious increase of S_{Mic} for C-25% $CaCO_3$ is attributed to the activation roles of alkaline CaO and CO_2 derived from the pyrolysis of $CaCO_3$ at 900 °C, which has been reported in our previous work[10]. When the content of $CaCO_3$ is further retained to 50% in the shrimp shell, the S_{BET} of resultant C-50% $CaCO_3$ decreases to 678.2 $m^2\ g^{-1}$, where S_{Mic} decreases sharply to 154.1 $m^2\ g^{-1}$ and S_{Mes} increases to about 2 times than that of C-25% $CaCO_3$. The results further imply that micropores collapse accompanied by formation of mesopores in C-50% $CaCO_3$ due to the excess activation by CaO and CO_2 at 900 °C. When pristine shrimp shell is used as the precursor, the resultant C-100% $CaCO_3$ shows further decreased both S_{Mic} (50.3 $m^2\ g^{-1}$) and S_{Mes} (339.9 $m^2\ g^{-1}$), which indicates that intrinsic $CaCO_3$ is the activator of the resultant mesoporous carbon. Particularly, an obvious increase in 0.9-1.0 p/p_0 indicates the presence of macropores for C-100% $CaCO_3$. Above results demonstrate that the original micropores and mesopores in C-25% $CaCO_3$ are further enlarged to mesopores and macropores in C-50% $CaCO_3$ and C-100% $CaCO_3$, respectively. The similar tendency of the obtained samples is also observed by the pore size distributions as shown in Fig. 4b. The pore sizes of the obtained carbons follow the order: C-25% $CaCO_3$ < C-50% $CaCO_3$ < C-100% $CaCO_3$. The gradual enlarged pores with the increased content of $CaCO_3$ indicate the activation role of CaO and CO_2. The ratios of S_{Mic}/S_{BET} are 0, 81.5%, 22.7%, 12.9% for C-0% $CaCO_3$, C-25% $CaCO_3$, C-50% $CaCO_3$ and C-100% $CaCO_3$, respectively. Furthermore, the ratios of V_{Mic}/V_{Total} with different $CaCO_3$ contents also exhibit

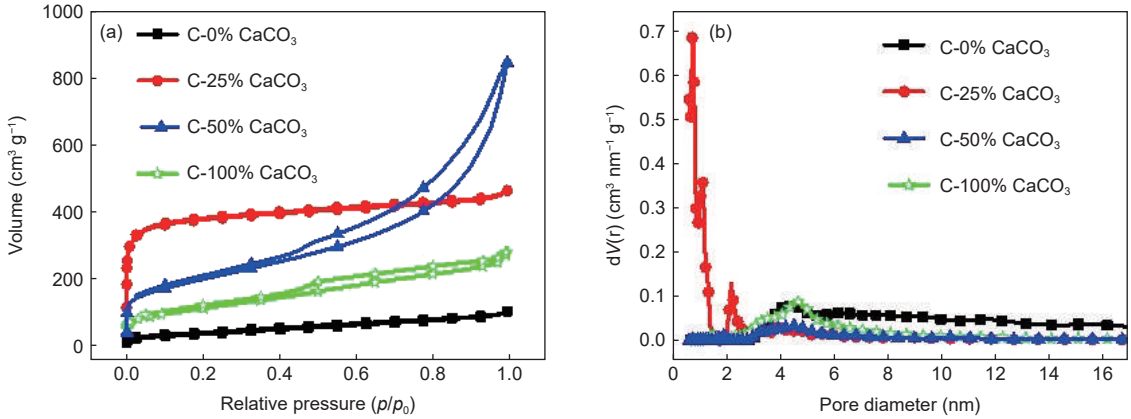

Fig. 4　(a) N_2 adsorption and desorption isotherms and (b) corresponding pore size distributions of C-0% $CaCO_3$, C-25% $CaCO_3$, C-50% $CaCO_3$ and C-100% $CaCO_3$ samples.

Table 1　Porous properties of the resultant carbons derived from shrimp shell.

Sample	S_{BET} ($m^2\ g^{-1}$)	S_{Mic} ($m^2\ g^{-1}$)	S_{Mec} ($m^2\ g^{-1}$)	S_{Mic}/S_{BET}	V_{Total} ($cm^3\ g^{-1}$)	V_{Mic} ($cm^3\ g^{-1}$)	V_{Mic}/V_{Total}	Pore size (nm)
C-0% $CaCO_3$	117.6	0	117.6	0%	0.14	0	0%	3.0-5.1
C-25% $CaCO_3$	1371.8	1114	257.8	81.5%	0.64	0.47	73.4%	0.5-2.5
C-50% $CaCO_3$	678.2	154.1	524.1	22.7%	0.51	0.16	33.4%	0.95-5.5
C-100%$CaCO_3$	390.2	50.3	339.9	12.9%	0.36	0.018	5.3%	1.5-5.0

Note: (a) S_{BET} is the specific surface area obtained from BET method, (b) S_{mic} is the microporous surface area calculated from t-plot method, (c) S_{mes} is the mesoporous surface area from t-method external surface area (S_{mes}=S_{BET}-S_{mic}) and (d) V_{total} is the total volume calculated at a relative pressure of 0.99.

the similar tendency. The results indicate that $CaCO_3$ derived from shrimp shell in the carbon precursor promotes the creation of micropores with the low content of $CaCO_3$ (< 25%), mesopores and macropores with increased contents of $CaCO_3$ (> 25%) for samples C-50% $CaCO_3$ and C-100% $CaCO_3$. Herein, CaO, as the new kind of activator derived from shrimp shell is very useful for the creation of porous carbon with various pore size, which is very different from the widely used corrosive activators such as KOH, H_3PO_4 and NaOH[29–31].

To obtain the chemical states of the surface elements, C-*X*% $CaCO_3$ (*X*=0, 25, 50, 100) samples are further analyzed by XPS spectra (Fig. 5) and corresponding quantitative analysis results are summarized in Table 2. The corresponding C1s spectra of the samples are shown in Fig. 5a. Three obvious peaks located at 284.6, 285.5 and 287.4 eV represent C—C/C=C, C—O, O—C=O functional groups, respectively. The peaks at 531.0 and 532.2 eV correspond to the C=O and C—O in the O 1s spectra, respectively (Fig. 5b). The N1s spectra of the samples are shown in Fig. 5c. The four peaks represent pyrrole nitrogen (N-5, 399.7 eV), pyridinium nitrogen (N-6, 398.0 eV), graphitized nitrogen (N-Q, 400.8 eV) and nitrogen oxide (N-X, 402.0 eV). It has been reported in the literature[32] that the functional groups N-5 and N-6 can provide the pseudocapacitance to facilitate the electrochemical performance of carbon. All samples exhibit the N-5 and N-6 contents in the range of 35.1%-41.7%. Particularly, the total amount of N-5 and N-6 of C-25% $CaCO_3$ sample can reach 18.3% and 17.8%, respectively. The contents of C, N and O in the samples are shown in Table 2. C-0% $CaCO_3$ sample contains about 83.8% C and 12.0% O. However, the C content increases while O content decreases for the obtained carbon when $CaCO_3$ remains in the carbon precursors. The maximum C content (88.0%) and least O content (8.4%) are achieved for C-25% $CaCO_3$ sample, whereas the O content increases with the increase of the content of $CaCO_3$, which can be attributed to an increased content of oxygen provided by CaO through activation. The N content barely changes for all the obtained samples except C-25% $CaCO_3$ which possesses the least N content of 3.6%.

The electrochemical performance of C-*X*% $CaCO_3$ (*X*=0, 25, 50 and 100) samples is tested in a

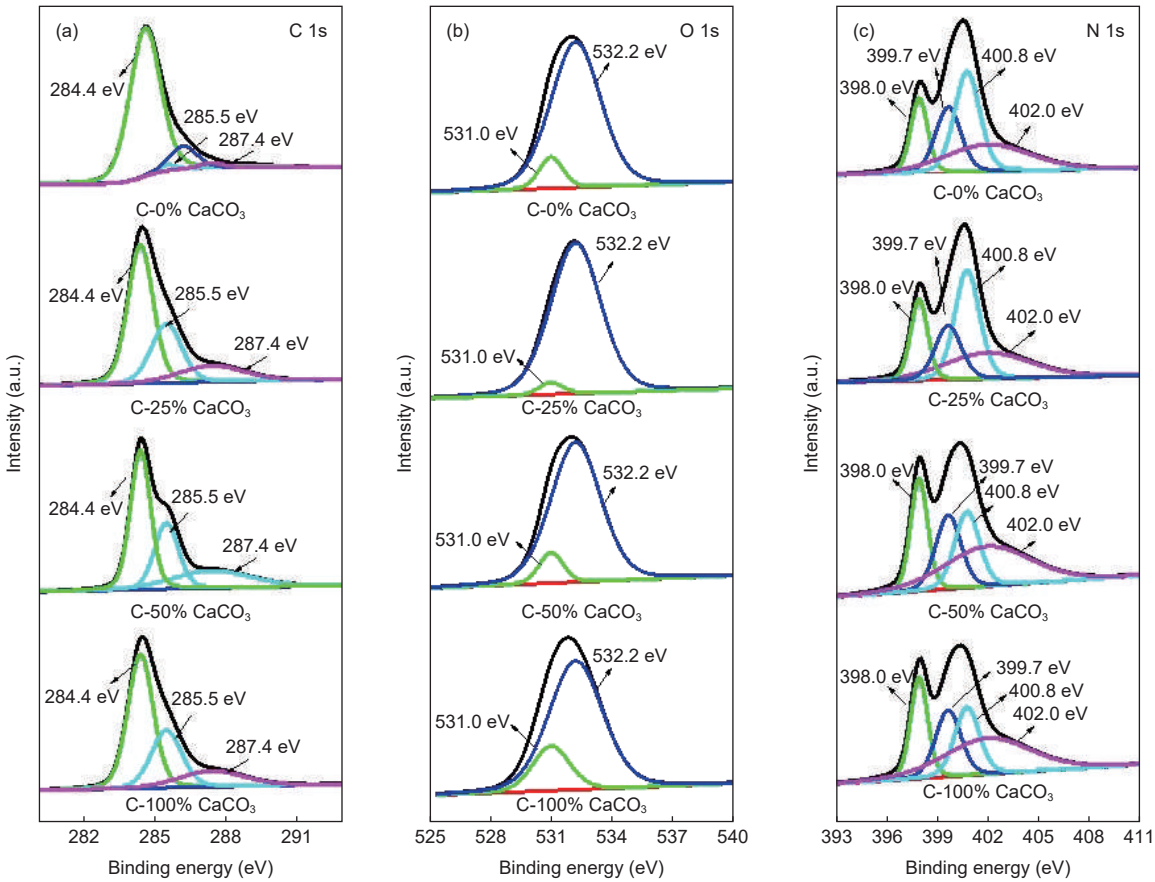

Fig. 5 XPS spectra of C-*X*% $CaCO_3$ (*X*=0, 25, 50 and 100) samples: (a) C 1s, (b) O 1s and (c) N 1s regions.

Table 2 The contents of N, C and O in the resultant carbons from XPS analysis.

Sample	XPS			N-6	N-5	N-Q	N-X	O-I	O-II
	C	N	O	398.0 eV	399.7 eV	400.8 eV	402.0 eV	531.0 eV	532.2 eV
C-0% $CaCO_3$	83.8%	4.2%	12.0%	21.1%	20.6%	20.6%	37.7%	92.0%	8.0%
C-25% $CaCO_3$	88.0%	3.6%	8.4%	17.8%	18.3%	35.0%	29.0%	25.8%	74.2%
C-50% $CaCO_3$	87.2%	4.1%	8.7%	16.3%	21.3%	32.6%	29.8%	9.5%	90.5%
C-100% $CaCO_3$	86.9%	4.0%	9.1%	15.1%	20.0%	34.6%	30.3%	19.2%	80.8%

three-electrode system with 6 mol L^{-1} KOH as the electrolyte. Fig. 6a exhibits a cyclic voltammetric curves of the samples. It is known that the C-25% $CaCO_3$ sample has the best electrochemical performance in all samples because of its largest area of the rectangular shape. Furthermore, the electrochemical performance of all the sample follows the order of C-25% $CaCO_3$>C-50% $CaCO_3$>C-100% $CaCO_3$>C-0% $CaCO_3$. The charge and discharge curves are shown in Fig. 6b. The samples all exhibit a good charge and discharge reversibility and the linear shape indicate the presence of EDLCs, where the porous structure dominates the final capacitance. The specific capacitances of the 4 samples follow the order as C-25% $CaCO_3$>C-50% $CaCO_3$>C-100% $CaCO_3$>C-0% $CaCO_3$ (Fig. 6c). Such order agrees with that of the surface areas, where the larger is surface area (or micro-surface area), the higher is the specific capacitance. Typically, the capacitances are respectively 273, 231, 186 and 90 F g^{-1} at a current density of 1 A g^{-1} for C-25% $CaCO_3$, C-50% $CaCO_3$, C-100% $CaCO_3$ and C-0% $CaCO_3$. Among them, C-25% $CaCO_3$ sample with the largest surface area has the highest specific capacitances of 328, 287, 281, 277, 273 and 266 F g^{-1} at 0.05, 0.1, 0.2, 0.5, 1.0 and 2.0 A g^{-1}, respectively. The performance is better than that of the reported N-containing ultra-microporous carbon (269 F g^{-1} at 1.0 A g^{-1})[33], oxygen-rich hierarchical porous carbon

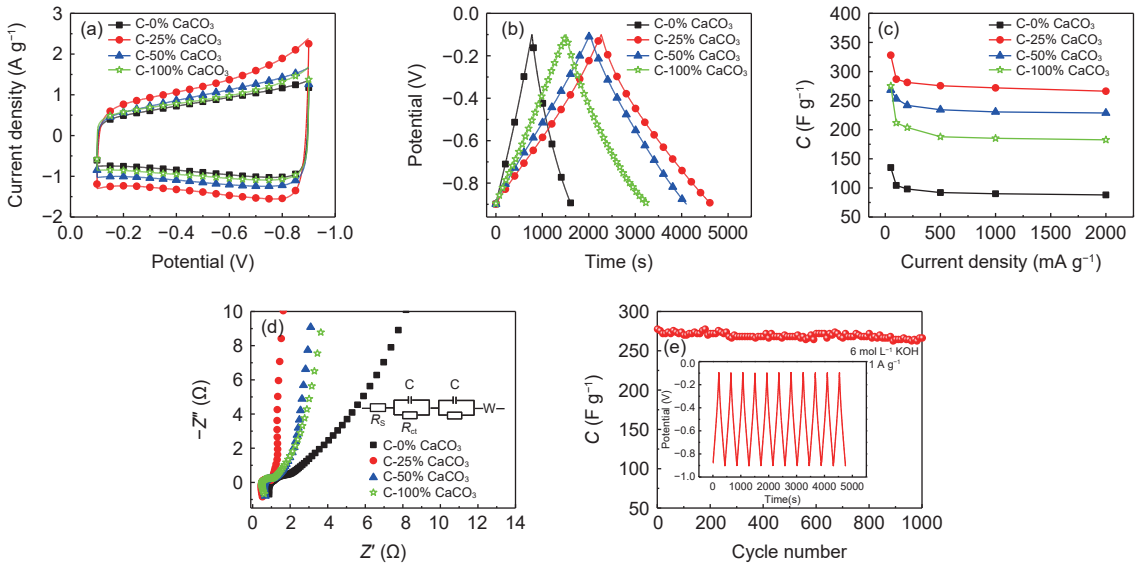

Fig. 6　Electrochemical characterizations of C-*X*% $CaCO_3$(*X*=0, 25, 50 and 100) samples measured in a three-electrolyte: (a) Cyclic voltammetry curves at a scan rate of 10 mV s^{-1}, (b) Galvanostatic charge-discharge curves of these samples at a current density of 100 mA g^{-1}, (c) Specific capacitances of carbon samples at different current densities, (d) Nyquist plots and (e) cycle performance of C-25% $CaCO_3$ electrode measured at a current density of 1 A g^{-1}, and the inset is the last 10 cycles of galvanostatic charge-discharge. All the above tests are conducted in a 6 mol L^{-1} KOH solution.

(222.6 F g^{-1} at 0.5 A g^{-1})[34], hierarchical porous carbons (188 F g^{-1} at 0.04 A g^{-1})[35], N-doped carbon (205 F g^{-1} at a current density of 0.5 A g^{-1})[36], N, P, S-codoped hierarchically porous carbon spheres (274 F g^{-1} at a current density of 0.5 A g^{-1})[37].

The EIS curves of the samples (Fig. 6d) are used to understand the capacitive nature of the samples by testing the ion transport behavior of the electrode materials. The half ring diameter in the high frequency region corresponds to the magnitude of the charge transfer resistance, while the oblique line in the low-mid frequency region is related to ion diffusion and capacitance characteristics[38]. The C-25% $CaCO_3$ sample exhibits a curve characteristic close to 90° in the low frequency region, indicating the sample has good capacitance performance[38]. The EIS equivalent circuit of the sample is shown in the inset of Fig. 6d. The circuit of the entire capacitor consists of R_s and R_{ct}. R_s is the sum of contact resistance and material resistance (including electrode material, electrolyte and current collector) and R_{ct} is a charge transfer resistance (corresponding to the adsorption-desorption of ions on the electrode material) and the fitting values are shown in Table 3. The R_{ct} of C-25% $CaCO_3$, C-50% $CaCO_3$, C-100% $CaCO_3$ and C-0% $CaCO_3$ samples are calculated to be 6.27, 1.55, 0.95 and 3.01 Ω, respectively. The above results indicate the carbon with a higher C content and less N/O content exhibits a better ion transport behavior and a lower charge transfer resistance, thereby improving the electrochemical performance. Fig. 6e shows the electrochemical curve of the sample cycled for 5 000 times at a current density of 1.0 A g^{-1}. The inset is the last 10 charge and discharge curves. The C-25% $CaCO_3$ sample has an excellent cycle stability with a retention of over 99% of the initial capacitance in this case.

The electrochemical performance tests are performed on C-*X*% $CaCO_3$ (*X*=0, 25, 50 and 100) samples under the three-electrode system with 1 mol L^{-1} H_2SO_4 as the electrolyte (Fig. 7). Fig. 7a shows the CV curves of the obtained materials at a scan rate of 10 mV s^{-1}. The electrochemical properties of all the samples are consistent with the conclusions at alkaline conditions as shown in Fig. 6, but the

Table 3　Kinetic parameters of the C-*X*% $CaCO_3$ electrodes.

Sample	R_s (Ω)	R_{ct} (Ω)
C-0% $CaCO_3$	0.72	6.27
C-25% $CaCO_3$	0.05	1.55
C-50% $CaCO_3$	1.03	0.95
C-100% $CaCO_3$	0.62	3.01

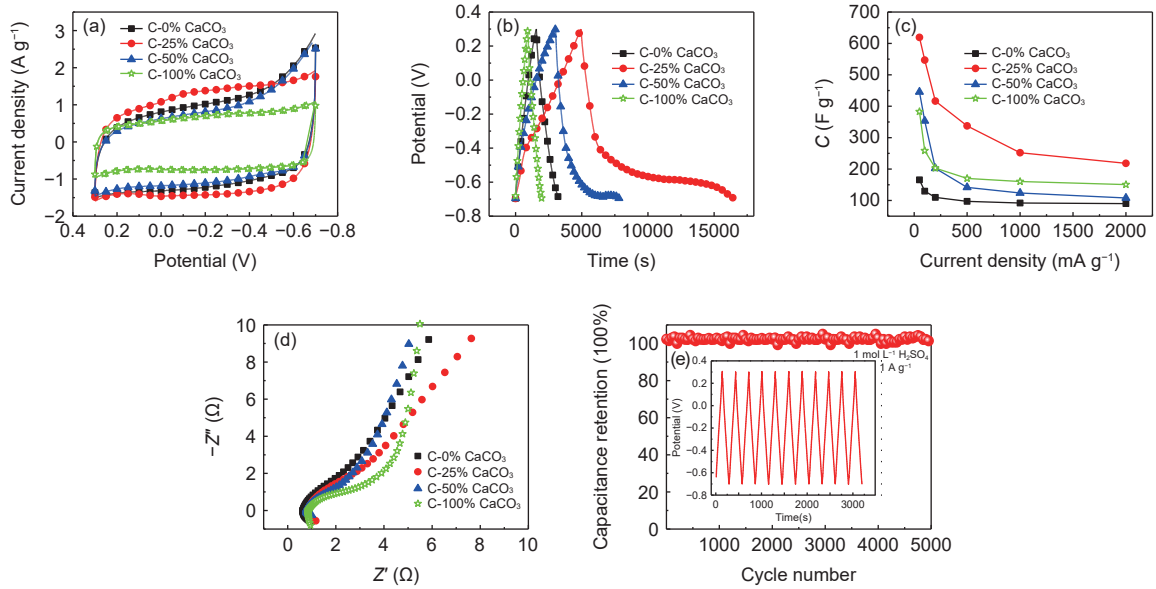

Fig. 7 Electrochemical characterizations of C-*X*% $CaCO_3$ (*X*=0, 25, 50 and 100) samples measured in a three-electrolyte: (a) CV curves at a scan rate of 10 mV s^{-1}, (b) Specific capacitances at different current densities, (c) Galvanostatic charge-discharge curves of these samples at a current density of 100 mA g^{-1}, (d) Nyquist plots and (e) cycle performance of C-25% $CaCO_3$ electrode measured at a current density of 1 A g^{-1}, and the inset is the last 10 cycles of galvanostatic charge-discharge. All the above tests are conducted in 1 mol L^{-1} H_2SO_4 solution.

apparent hump at low voltages indicates the redox capacitance derived from the presence of N-/O-functional groups. The irregular linear shape of the curves (Fig. 7b) further indicates the presence of redox capacitance. The results demonstrate that doped N and O heteroatoms contribute lots for the redox capacitance in the H_2SO_4 electrolyte. The specific capacitance curves at different current densities are shown in Fig. 7c. At the current density of 0.05 A g^{-1}, the specific capacitances of C-25% $CaCO_3$, C-50% $CaCO_3$, C-100% $CaCO_3$ and C-0% $CaCO_3$ are 619, 446, 382 and 166 F g^{-1}, respectively. It is obvious that the specific capacitances under acidic conditions are significantly higher than that in the alkaline electrolyte, which is attributed to the redox capacitance provided by appropriate N/O contents. However, the specific capacitance of the samples has a significant decrease after the current density is higher than 0.5 A g^{-1} due to the large hindrance of ion transport by micropores in the acidic system. As a result, the capacitance of C-25% $CaCO_3$ sample decreases from 619.2 at 0.05 A g^{-1} to 252 F g^{-1} at 1 A g^{-1}. The EIS curves (Fig. 7d) show that all samples in the acidic system exhibit a curve characteristic close to 90° in the low frequency region, indicating the good ion transport behavior in this case. Fig. 7e shows the electrochemical curve of the sample cycled 5 000 times at a current density of 1 A g^{-1}, where the capacitance of C-25% $CaCO_3$ sample is still up to 266 F g^{-1}, maintaining a capacitance of 96.0% of its initial. The C-25% $CaCO_3$ sample exhibits the excellent rate performance and the high cycle stability.

The C-100% $CaCO_3$ and C-25% $CaCO_3$ samples are electrochemically tested in a 6 mol L^{-1} KOH electrolyte in a symmetric two-electrode system, as shown in Fig. 8. The good capacitance behavior of the two samples in the wide voltage range of 0-1.0 V can be concluded by the CV curves (Fig. 8a). The CV curve of the C-25% $CaCO_3$ shows better rectangular shape and larger area than that of the C-100% $CaCO_3$, which means the better electrochemical performance of C-25% $CaCO_3$. The galvanostatic charge/discharge curves of symmetrical supercapacitors at 50 mA g^{-1} look mostly symmetrical with a slight curvature (Fig. 8b), indicating some pseudocapacitive contribution along with the EDL contribution[7, 39]. The EIS curves of the C-100% $CaCO_3$ and C-25% $CaCO_3$ samples are shown in Fig. 8c. The C-25% $CaCO_3$ sample has a smaller semicircle diameter than C-100% $CaCO_3$. It is attributed to the importance of the porous structure to ion diffusion when the sample has

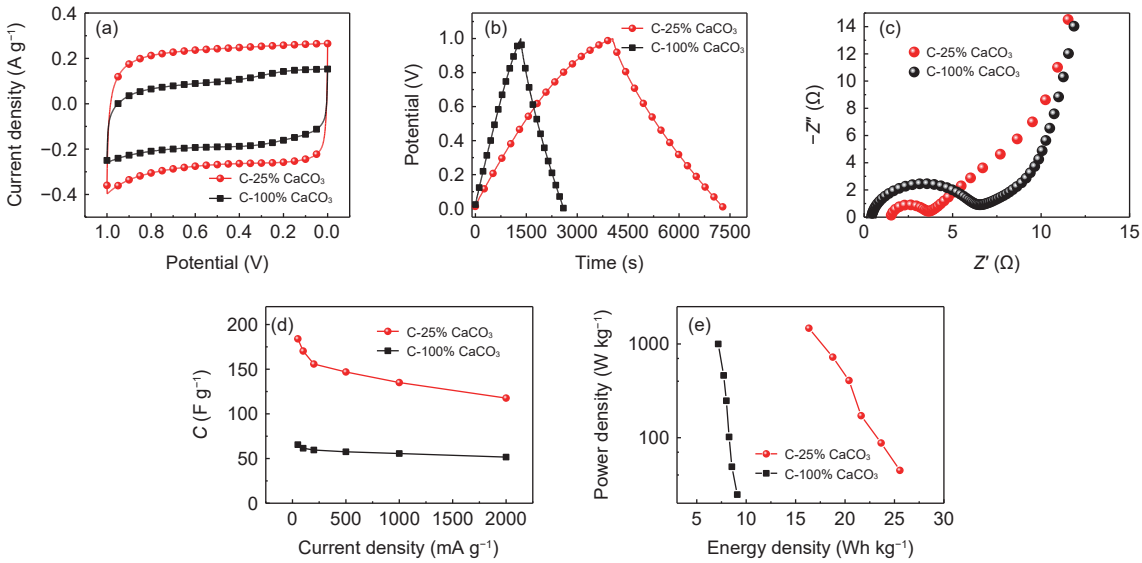

Fig. 8　Electrochemical performance of C-100% $CaCO_3$ and C-25% $CaCO_3$ samples as supercapacitor electrodes in a two-electrode symmetric cell configuration in 6 mol L^{-1} KOH: (a) CV curves at 10 mV s^{-1}, (b) Galvanostatic charge-discharge curves at 50 mA g^{-1}, (c) Nyquist plots, (d) Specific capacitances at different current density and (e) power density vs. energy density.

a similar nitrogen content. Fig. 8d shows the specific capacitance in a symmetric two-electrode system. According to the total mass of the two electrodes, the specific capacitances of C-100% $CaCO_3$ and C-25% $CaCO_3$ samples at 0.05 A g^{-1} are 65.5 and 184.0 F g^{-1}, respectively, where the latter is about twice than that of the former. The energy density-power density curves of the samples are shown in Fig. 8e. The energy densities of the C-100% $CaCO_3$ and C-25% $CaCO_3$ samples are determined to be 9.0 and 26.0 Wh kg^{-1} with power densities of 1 000 and 1 470.9 W kg^{-1} respectively. Our results are significantly higher than that of the reported activated carbon (5.1 Wh kg^{-1})[40], hierarchical porous carbon (20.1 Wh kg^{-1})[41], and white clover carbons (25.0-13.1 Wh kg^{-1})[42] (Table 4).

Table 4　Supercapacitor performance comparison of carbon materials.

Raw material	Synthesis method	Energy densities (Wh kg^{-1})	Reference
Shrimp shells	self-template and self-activator	26.0	This work
Rice husk	NaOH activation	5.1	[40]
Cauliflower	KOH activation	20.5	[43]
Corncob	KOH activation	20.1	[41]
White clover	$ZnCl_2$ activation	13.1-25.0	[42]
Shrimp shells	H_3PO_4 activation	5.2	[23]
Loofah sponge	KOH activation	16.1	[44]
Wool fiber	LiCl/KCl/KNO_3	20.1	[45]

4　Conclusions

In summary, nitrogen-doped porous carbons have been synthesized with adjustable pores using shrimp shell as the carbon/nitrogen source, the $CaCO_3$ component as both the template and activator. The process is very efficient and sustainable, where intrinsic $CaCO_3$ in shrimp shell plays the role of the activator and the template. The resulting samples have ultrahigh specific surface area and abundant pores, which show the high capacitance (328 F g^{-1} at 0.05 A g^{-1} in KOH), long cycle life, high energy and power densities. The shrimp shell as the waste is cheap and easy to obtain, and it enables the high-value-added utilization of waste.

Acknowledgements

This work is supported by the NSFC (No. 51972059, 51901043), Scientific Research Foundation for Leading Scholars in Dongguan University of Technology (DGUT) (GB200902-31), and Research Start-up Funds of DGUT (GC300501-072).

References

[1] Sun J, Li P, Qu J, et al. Electricity generation from a Ni-Al layered double hydroxide-based flexible generator driven by natural water evaporation[J]. Nano Energy, 2019, 57: 269-278.

[2] Wang Q, Yan J, Fan Z. Carbon materials for high volumetric

performance supercapacitors: Design, progress, challenges and opportunities[J]. Energy Environmental Science, 2016, 9(3): 729-762.

[3] Wang Y, Song Y, Xia Y. Electrochemical capacitors: Mechanism, materials, systems, characterization and applications[J]. Chemical Society Reviews, 2016, 45(21): 5925-5950.

[4] Shao Y, El-Kady M F, Sun J, et al. Design and mechanisms of asymmetric supercapacitors[J]. Chemical Reviews, 2018, 118(18): 9233-9280.

[5] Zhao Y, Yu Y, Lv C X, et al. A high energy density fiber-shaped supercapacitor based on zinc-cobalt bimetallic oxide nanowire forests on carbon nanotube fibers[J]. New Carbon Materials, 2019, 34(6): 559-568.

[6] Xu G, Han J, Bing D, et al. Biomass-derived porous carbon materials with sulfur and nitrogen dual-doping for energy storage[J]. Green Chemistry, 2015, 17(3): 1668-1674.

[7] He X, Zhang N, Shao X, et al. A layered-template-nanospace-confinement strategy for production of corrugated graphene nanosheets from petroleum pitch for supercapacitors[J]. Chemical Engineering Journal, 2016, 297: 121-127.

[8] Wei J, Luo C, Li H, et al. Direct assembly of micron-size porous graphene spheres with a high density as supercapacitor materials[J]. Carbon, 2019, 149: 492-498.

[9] Kai W, Chao G, Li S E, et al. Electrochemical performance of high surface area activated carbons derived from coal tar pitch[J]. New Carbon Materials, 2018, 33(6): 562-570.

[10] Gao F, Geng C, Xiao N, et al. Hierarchical porous carbon sheets derived from biomass containing an activation agent and in-built template for lithium ion batteries[J]. Carbon, 2018, 139: 1085-1092.

[11] Liu M, Niu J, Zhang Z, et al. Potassium compound-assistant synthesis of multi-heteroatom doped ultrathin porous carbon nanosheets for high performance supercapacitors[J]. Nano Energy, 2018, 51: 366-372.

[12] Peng X, Gao F, Zhao J, et al. Self-assembly of a graphene oxide/$MnFe_2O_4$ motor by coupling shear force with capillarity for removal of toxic heavy metals[J]. Journal of Materials Chemistry A, 2018, 6(42): 20861-20868.

[13] He X, Ling P, Qiu J, et al. Efficient preparation of biomass-based mesoporous carbons for supercapacitors with both high energy density and high power density[J]. Journal of Power Sources, 2013, 240: 109-113.

[14] Zhang Q H, Zuo S L, Wei X Y, et al. H_3PO_4 activated carbons as the electrode materials of supercapacitors using an ionic liquid electrolyte[J]. New Carbon Materials, 2018, 33(1): 61-70.

[15] Cao D, Zhang Q, Hafez A M, et al. Lignin-derived holey, layered, and thermally conductive 3D scaffold for lithium dendrite suppression[J]. Small Methods, 2019, 3(5): 1800539-1800549.

[16] Hu Y S, Adelhelm P, Smarsly B M, et al. Synthesis of hierarchically porous carbon monoliths with highly ordered microstructure and their application in rechargeable lithium batteries with high-rate capability[J]. Advanced Functional Materials, 2010, 17(12): 1873-1878.

[17] Xu G, Ding B, Shen L, et al. Sulfur embedded in metal organic framework-derived hierarchically porous carbon nanoplates for high performance lithium-sulfur battery[J]. Jouranl of Materials Chemistry A, 2013, 1(14): 4490-4496.

[18] He X, Li X, Ma H, et al. ZnO template strategy for the synthesis of 3D interconnected graphene nanocapsules from coal tar pitch as supercapacitor electrode materials[J]. Journal of Power Sources, 2017, 340: 183-191.

[19] Feng W, zhang H F, He X J, et al. Synthesis of porous carbons from coal tar pitch for high-performance supercapacitors[J]. New Carbon Materials, 2019, 34(2): 132-139.

[20] Qiu D, Cao T, Zhang J, et al. Precise carbon structure control by salt template for high performance sodium-ion storage[J]. Journal of Energy Chemistry, 2019, 31: 101-106.

[21] Guo H, Bing D, Jie W, et al. Template-induced self-activation route for nitrogen-doped hierarchically porous carbon spheres for electric double layer capacitors[J]. Carbon, 2018, 136: 204-210.

[22] White R J, Antonietti MTitirici M M. Naturally inspired nitrogen doped porous carbon[J]. Journal of Materials Chemistry, 2009, 19(45): 8645-8650.

[23] Qu J, Geng C, Lv S, et al. Nitrogen, oxygen and phosphorus decorated porous carbons derived from shrimp shells for supercapacitors[J]. Electrochim Acta, 2015, 176: 982-988.

[24] Gao F, Qu J Y, Geng C, et al. Self-templating synthesis of nitrogen-decorated hierarchical porous carbon from shrimp shell for supercapacitors[J]. Journal of Materials Chemistry A, 2016, 4(19): 7445-7452.

[25] Gao F, Qu J, Zhao Z, et al. Nitrogen-doped activated carbon derived from prawn shells for high-performance supercapacitors[J]. Electrochim Acta, 2016, 190: 1134-1141.

[26] Xiao C, Zhang W, Lin H, et al. Modification of a rice husk-based activated carbon by thermal treatment and its effect on its electrochemical performance as a supercapacitor electrode[J]. New Carbon Materials, 2019, 34(4): 341-348.

[27] Tajima T, Tsutsui A, Fujii T, et al. Fabrication of novel core-shell microspheres consisting of single-walled carbon nanotubes and $CaCO_3$ through biomimetic mineralization[J]. Polymer Jouranl, 2012, 44(6): 620-624.

[28] Liu H, Cao C, Wei F, et al. Fabrication of macroporous/mesoporous carbon nanofiber using $CaCO_3$ nanoparticles as dual purpose template and its application as catalyst support[J]. The Journal of Physical Chemistry C, 2013, 117(41): 21426-21432.

[29] Huanlei W, Zhanwei X, Alireza K, et al. Interconnected carbon nanosheets derived from hemp for ultrafast supercapacitors with high energy[J]. ACS Nano, 2013, 7(6): 5131-5141.

[30] Mahasweta N, Keisuke O, Arghya D, et al. Unprecedented CO_2 uptake over highly porous N-doped activated carbon monoliths prepared by physical activation[J]. Chemical Communications, 2012, 48(83): 10283-10285.

[31] Laine J, Calafat A, Labady M. Preparation and characterization of activated carbons from coconut shell impregnated with phosphoric

acid[J]. Carbon, 1989, 27(2): 191-195.

[32] Liu H, Song H, Chen X, et al. Effects of nitrogen- and oxygen-containing functional groups of activated carbon nanotubes on the electrochemical performance in supercapacitors[J]. Journal of Power Sources, 2015, 285: 303-309.

[33] Lu W, Liu M, Ling M, et al. Nitrogen-containing ultramicroporous carbon nanospheres for high performance supercapacitor electrodes[J]. Electrochim Acta, 2016, 205: 132-141.

[34] Li J, Liu W, Xiao D, et al. Oxygen-rich hierarchical porous carbon made from pomelo peel fiber as electrode material for supercapacitor[J]. Applied Surface Science, 2017, 416: 918-924.

[35] Kang W, Lin B, Huang G, et al. Peanut bran derived hierarchical porous carbon for supercapacitor[J]. Journal of Materials Science - Materials in Electronics, 2018, 29(8): 6361-6368.

[36] Cheng L, Yu H, Yong J, et al. Camellia pollen-derived carbon for supercapacitor electrode material[J]. Journal of Power Sources, 2018, 394: 9-16.

[37] Yan L, Li D, Yan T, et al. Catalytic transfer hydrogenolysis of lignin-derived aromatic ethers promoted by bimetallic Pd/Ni systems[J]. ACS Sustainable Chemistry & Engineering, 2018, 6(7): 5265-5272.

[38] Zhang Z, Zhou Z, Peng H, et al. Nitrogen- and oxygen-containing hierarchical porous carbon frameworks for high-performance supercapacitors[J]. Electrochim Acta, 2014, 134(21): 471-477.

[39] He X, Zhao N, Qiu J, et al. Synthesis of hierarchical porous carbons for supercapacitors from coal tar pitch with nano-Fe_2O_3 as template and activation agent coupled with KOH activation[J]. Journal of Materials Chemistry A, 2013, 1(33): 9440-9450.

[40] Teo E, Muniandy L, Ng E, et al. High surface area activated carbon from rice husk as a high performance supercapacitor electrode[J]. Electrochim Acta, 2016, 192: 110-119.

[41] Yang S, Zhang K. Converting corncob to activated porous carbon for supercapacitor application[J]. Nanomaterials, 2018, 8(4): 181-191.

[42] Ma G, Zhang Z, Sun K, et al. White clover based nitrogen-doped porous carbon for a high energy density supercapacitor electrode[J]. Rsc Advances, 2015, 5(130): 107707-107715.

[43] Men B, Guo P, Sun Y, et al. High-performance nitrogen-doped hierarchical porous carbon derived from cauliflower for advanced supercapacitors[J]. Journal of Materials Science, 2018, 54(3): 2446-2457.

[44] Su X, Chen J, Zheng G, et al. Three-dimensional porous activated carbon derived from loofah sponge biomass for supercapacitor applications[J]. Applied Surface Science, 2018, 436: 327-336.

[45] Zeng D, Dou Y, Li M, et al. Wool fiber-derived nitrogen-doped porous carbon prepared from molten salt carbonization method for supercapacitor application[J]. Journal of Materials Science, 2018, 53(11): 8372-8384.